

JGR Solid Earth

RESEARCH ARTICLE

10.1029/2022JB024321

Key Points:

- The 2021 M_w 6.0 Yangbi earthquake involved unilateral rupture on an unmapped strike-slip fault with no surface offset
- Directivity analysis shows that the rupture propagated southeast \sim 8.0 km with rupture velocity of \sim 2.2 km/s and a peak slip of \sim 2.1 m
- Foreshocks and aftershocks are distributed near margins of the main slip area, suggesting substantial stress drop during the mainshock

Supporting Information:

Supporting Information may be found in the online version of this article.

Correspondence to:

L. Ye,
yell@sustech.edu.cn

Citation:

Gong, W., Ye, L., Qiu, Y., Lay, T., & Kanamori, H. (2022). Rupture directivity of the 2021 M_w 6.0 Yangbi, Yunnan Earthquake. *Journal of Geophysical Research: Solid Earth*, 127, e2022JB024321. <https://doi.org/10.1029/2022JB024321>

Received 2 MAR 2022

Accepted 1 SEP 2022

Author Contributions:

Conceptualization: Lingling Ye
Data curation: Wenzheng Gong
Formal analysis: Wenzheng Gong, Yuxin Qiu
Investigation: Wenzheng Gong, Lingling Ye, Thorne Lay, Hiroo Kanamori
Methodology: Wenzheng Gong, Lingling Ye, Yuxin Qiu
Supervision: Lingling Ye, Thorne Lay, Hiroo Kanamori
Writing – original draft: Wenzheng Gong
Writing – review & editing: Wenzheng Gong, Lingling Ye, Yuxin Qiu, Thorne Lay, Hiroo Kanamori

© 2022. American Geophysical Union.
All Rights Reserved.

Rupture Directivity of the 2021 M_w 6.0 Yangbi, Yunnan Earthquake

Wenzheng Gong¹ , Lingling Ye¹ , Yuxin Qiu¹, Thorne Lay² , and Hiroo Kanamori³ 

¹Department of Earth and Space Sciences, Southern University of Science and Technology, Shenzhen, China, ²Department of Earth and Planetary Sciences, University of California Santa Cruz, Santa Cruz, CA, USA, ³Seismological Laboratory, California Institute of Technology, Pasadena, CA, USA

Abstract The 2021 M_w 6.0 Yangbi, Yunnan strike-slip earthquake occurred on an unmapped crustal fault near the Weixi-Qiaoho-Weishan Fault along the southeast margin of the Tibetan Plateau. Using near-source broadband seismic data from ChinArray, we investigate the spatial and temporal rupture evolution of the mainshock using apparent moment-rate functions (AMRFs) determined by the empirical Green's function (EGF) method. Assuming a 1D line source on the fault plane, the rupture propagated unilaterally southeastward (\sim 144°) over a rupture length of \sim 8.0 km with an estimated rupture speed of 2.1 km/s to 2.4 km/s. A 2D coseismic slip distribution for an assumed maximum rupture propagation speed of 2.2 km/s indicates that the rupture propagated to the southeast \sim 8.0 km along strike and \sim 5.0 km downdip with a peak slip of \sim 2.1 m before stopping near the largest foreshock, where three bifurcating subfaults intersect. Using the AMRFs, the radiated energy of the mainshock is estimated as \sim 1.6 \times 10¹³ J. The relatively low moment scaled radiated energy E_R/M_0 of 1.5×10^{-5} and intense foreshock and aftershock activity might indicate reactivation of an immature fault. The earthquake sequence is mainly distributed along a northwest-southeast trend, and aftershocks and foreshocks are distributed near the periphery of the mainshock large-slip area, suggesting that the stress in the mainshock slip zone is significantly reduced to below the level for more than a few overlapping aftershock to occur.

Plain Language Summary On 21 May 2021, an M_w 6.0 strike-slip earthquake occurred in the Yangbi region, Yunnan, China, near the southeast margin of the Tibetan Plateau. It is the largest earthquake in recent decades in the Yangbi region and caused 3 deaths. Due to southeastward extrusion of the Tibetan Plateau, there are several active faults in the Yangbi region with numerous moderate and small earthquakes, but no previously identified fault at the 2021 epicenter. To understand the mechanism of the 2021 Yangbi earthquake and the potential hazard in this region, we investigate the rupture process using nearby broadband seismic recordings from ChinArray. We find that the Yangbi earthquake propagated to the southeast \sim 8.0 km along strike and \sim 5.0 km downdip with rupture speed of 2.2 km/s. It stopped near the location of three bifurcating subfaults to the southeast, where diffuse faulting may have hindered further rupture propagation. We estimate the total radiated energy due to the dynamic rupture and find relatively low radiated seismic energy for the mainshock size, suggesting that the rupture occurred on an immature fault. There are few aftershocks and foreshocks within the mainshock slip area, suggesting substantial release of accumulated stress.

1. Introduction

On 21 May 2021 at 21:48:35 (Beijing time, UTC+8), an M_s 6.4 earthquake struck the Yangbi Yi Autonomous County region in Yunnan province, southwest China [hypocenter at 25.67°N, 99.87°E, 8.0 km deep; based on the earthquake catalog provided by Yunnan Earthquake Agency (YEA)]. This is the largest earthquake in recent decades in the Yangbi region (Figure 1). The focal mechanism indicates right-lateral strike-slip slip on a steeply dipping, northwest-southeast trending fault that was not previously mapped and for which no surface rupture occurred. The event caused 3 deaths and 28 injuries, with an estimated damage loss of 310 million CNY (\sim 48 million US\$). There have been diffuse moderate and small earthquakes near the Yangbi sequence with several M6.0+ events widely distributed north and east of the 2021 mainshock, the largest one being an M_s 7.0 event in 1925 [Figure 2a; M_s 7.0 from the China Earthquake Network Center (CENC) catalog and M_w 6.9 from the ISC-GEM catalog: <https://earthquake.usgs.gov/earthquakes/eventpage/iscgem910412/origin/detail>]. Interesting characteristics of the faulting and spatiotemporal distribution of the earthquake sequence prompt us to investigate

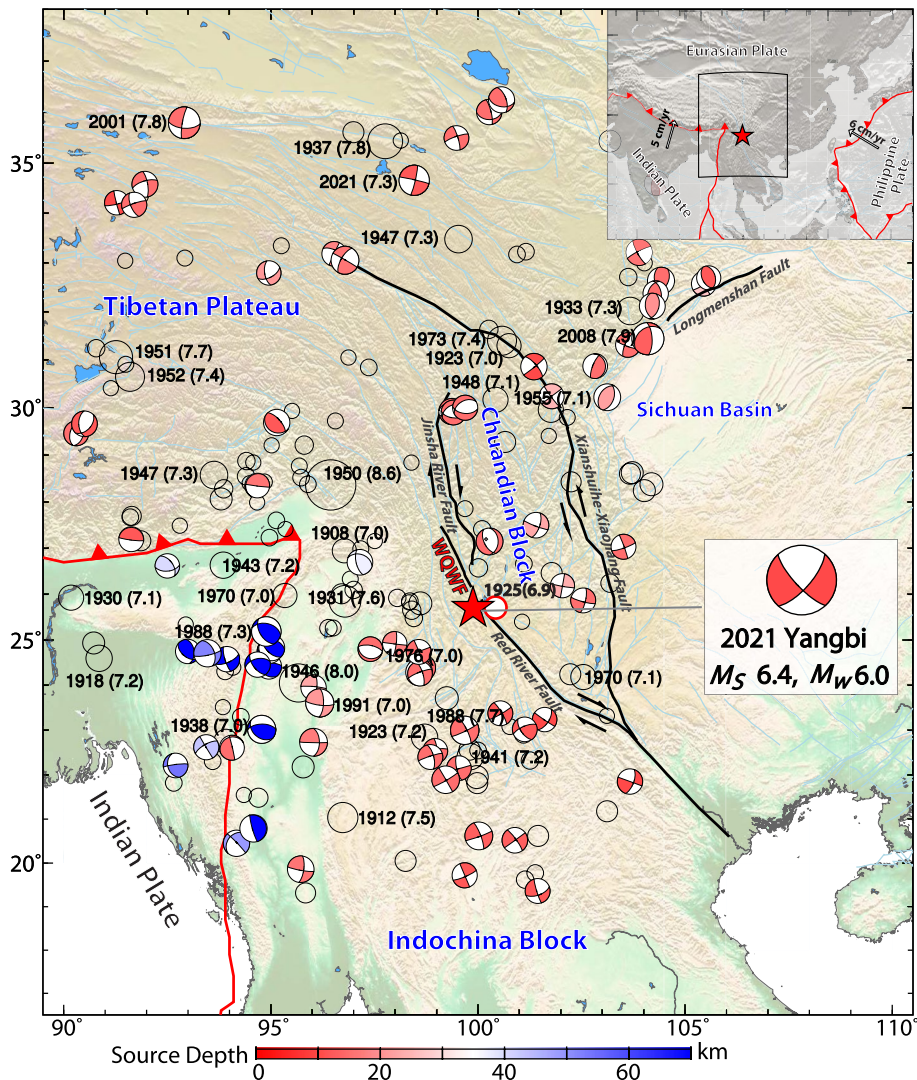


Figure 1. Tectonic setting and large earthquakes around the 2021 M_w 6.0 Yangbi, Yunnan earthquake near the margin of the southeast Tibetan Plateau. Historical seismicity with magnitude ≥ 6.0 from the U.S. Geological Survey National Earthquake Information Center (USGS-NEIC) catalog from 1900 to 1976 and from the GCMT catalog since 1976 are shown as black circles and focal mechanisms color-coded with source depth, respectively. Major historical events with magnitude ≥ 7.0 are labeled by the occurrence year and magnitude. Black lines show major active faults from the China Earthquake Data Center (<http://datashare.igl.earthquake.cn/map/ActiveFault/introFault.html>) (WQWF: Weixi-Qiaohou-Weishan Fault). The red star shows the epicenter of the 2021 Yangbi earthquake from the catalog provided by Yunnan Earthquake Agency (YEA). The inset map at the top right shows the regional plate tectonic setting with arrows indicating plate motion direction and rate relative to a fixed Eurasian plate computed using model NUVEL-1 (Argus & Gordon, 1991).

the mechanism of the 2021 Yangbi sequence and rupture process of the mainshock using numerous available regional seismic recordings (Figure 2b).

The 2021 M_s 6.4 Yangbi earthquake was preceded by numerous foreshocks, including several M3 - M4 events in the YEA catalog beginning 3 days ahead (Figures 2c and 2d), and the largest foreshock with M_s 5.6 occurred ~ 27 min before the mainshock. More than 4300 aftershocks have been reported up to 9 June, and the largest aftershock with M_s 5.3 occurred ~ 43 min after the mainshock. This vigorous earthquake sequence is mainly distributed along a northwest-southeast trend (Figure 2c), parallel to and offset toward the west by about 10 km from the mapped Weixi-Qiaohou-Weishan (WQW) fault (Figure 2a), although some aftershocks occurred along a minor NE trending lineation. High-resolution relocation studies (e.g., Duan et al., 2021; Lei et al., 2021; Liu et al., 2022; Su et al., 2021; Wang, Liu, et al., 2021; Zhang et al., 2021; Zhou et al., 2021) indicate that the sequence occurred

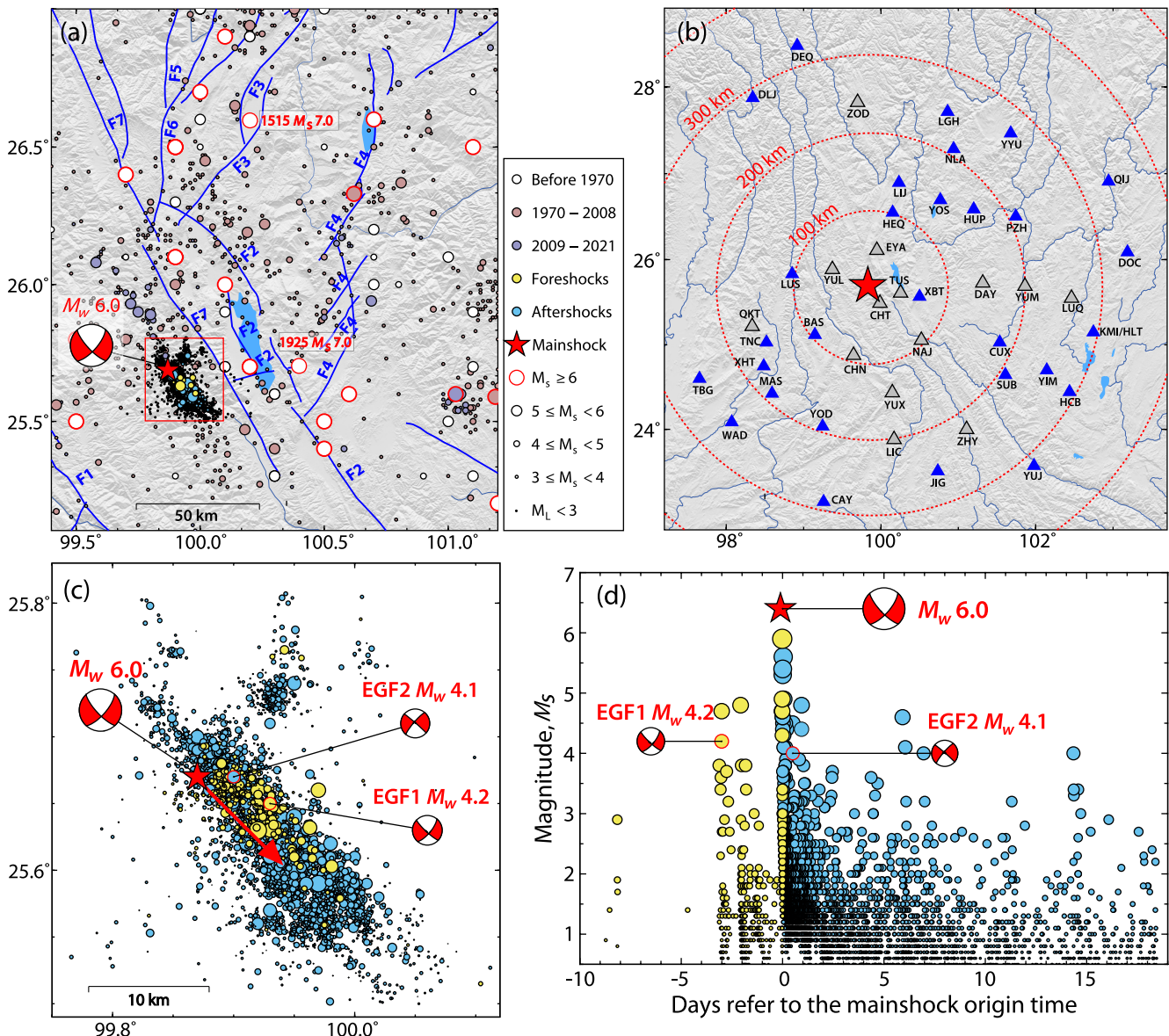


Figure 2. Background seismicity, station distribution, and the 2021 Yangbi earthquake sequence. (a) Background seismicity around the 2021 Yangbi sequence from the China Earthquake Network Center (CENC) catalog (<http://www.ceic.ac.cn/history>). The red rectangle indicates the area of the Yangbi sequence plotted in (c) and (d) with the red star showing the epicenter from Yunnan Earthquake Agency (YEA) and the focal mechanism being from our CAP inversion for the mainshock. Thick blue lines show major active faults from Deng et al. (2007); F1: Lancang River fault; F2: Red River fault system; F3: Heping-Eryuan fault; F4: Yongsheng-Binchuan fault system; F5: Jinshajiang fault; F6: Longpan-Qiaohou fault; and F7: Weixi-Weishan fault (~10 km east from the Yangbi sequence). (b) Near-source broadband station distribution used in this study. Recordings from all stations are used to invert focal mechanisms of the mainshock and EGFs. Some stations (blue triangles) with high-quality SH wave recordings are used in the deconvolution for the apparent moment-rate functions. (c) Spatial distribution for the 2021 Yangbi sequence from the YEA catalog. The red arrow indicates the rupture direction of the mainshock. Yellow and blue circles show foreshocks (including EGF1) and aftershocks (including EGF2), respectively. The CAP mechanisms of the mainshock and the two EGF events are shown with tie lines to their respective epicenters. (d) Temporal evolution for the 2021 Yangbi sequence, beginning with several M4 foreshocks 3 days ahead in a strong foreshock sequence, and followed by intensive aftershock activity over several weeks.

on an unmapped conjugate fault system. The mainshock is located at the northwest end of the NW-trending distribution, foreshocks are mainly concentrated in the northwest and central region, while aftershocks are distributed more widely. There appear to be three quasi-parallel subfaults in the southeast part of the NW trending distribution from well-calibrated catalogs such as those by Long et al. (2021) and Wang, Liu, et al. (2021) (see Figure 11).

The 2021 Yangbi sequence occurred near the southwest boundary of the Sichuan-Yunnan block along the southeast margin of the Tibetan Plateau in China (Figure 1). The unmapped fault system hosting the Yangbi sequence

is within the minor Lanping-Simao block, which is a region of stress concentration near the intersection of the Red River fault zone and the Lijiang-Dali fault system (Wang, Liu, et al., 2021). To the north and east of the Yangbi sequence, there are several NNW to NW trending faults including the WQW fault and NE trending faults such as the Heqing-Eryuan fault (Figure 2a). NNW to NW trending faults with sinistral strike-slip and thrust faulting components were formed in this region during the early stage of the Himalayan tectonic movement in the Oligocene (Leloup et al., 1995). During the late stage of Himalayan evolution in the Pliocene, the east-west compressional tectonic stress changed to an approximately north-south direction, causing the NNW to NW trending faults to change motion to dextral strike-slip or normal faulting components (Cui et al., 2006). Wang, Liu, et al. (2021) suggest that the unmapped fault on which the Yangbi sequence occurred was originally on a NW trending sinistral strike-slip, reactivated with dextral strike-slip motion due to resistance of the Lanping-Simao block to north-south expulsion of Tibetan Plateau material to the southeast (Wang & Shen, 2020; Zhang et al., 2013). According to Wang et al. (2008), the WQW fault has a relatively low strike-slip slip rate of 1–3 mm/yr, and a very low slip rate is expected for the fault that ruptured in 2021 as there was very little activity in the fault zone and no mapped surface trace prior to this event. Sun et al. (2022) suggest that upward migration of fluids and possibly melt below the source region could have weakened a locked asperity, triggering the 2021 Yangbi earthquake. Lei et al. (2021) investigate the effects of tidal modulation on the Yangbi sequence and suggest that the 2021 Yangbi earthquake sequence was significantly affected by the action of deep fluids.

To better understand the mechanism of the 2021 Yangbi sequence and the potential hazard around the unmapped fault, we study the rupture process of the mainshock. We extract apparent moment rate functions (AMRFs) from near-source broadband seismic data (Figure 2b) using the empirical Green's function (EGF) method. Then, we estimate rupture direction, rupture speed, and rupture length assuming a 1D line source by modeling the AMRFs. With constraints from the line source, we invert for the coseismic slip distribution on a 2D fault plane using a non-negative linear least squares (NNLSQ) method. Furthermore, we discuss the relationship between the slip and aftershocks (and foreshocks), stress change, and estimate the radiated energy based on AMRFs to understand the rupture characteristics of the unmapped fault.

2. Methods and Results

2.1. Point-Source Focal Mechanisms

Several agencies reported the focal mechanism of the M_s 6.4 mainshock rapidly, based on global teleseismic waveforms or regional recordings. The U.S. Geological Survey National Earthquake Information Center (USGS-NEIC) very long-period W -phase inversion has a double-couple solution with strike $\phi = 135^\circ$, dip $\delta = 82^\circ$, and rake $\lambda = -165^\circ$ with seismic moment $M_0 = 1.743 \times 10^{18} \text{ N} \cdot \text{m}$ (M_{WW} 6.09), and centroid depth at 17.5 km (<https://earthquake.usgs.gov/earthquakes/eventpage/us7000e532/moment-tensor>). The Global Centroid Moment Tensor (GCMT) solution, based on a dataset of 332 body waves, 197 mantle waves, and 391 surface waves lowpass filtered at periods of 40, 125, and 50 s, respectively, has a best double-couple with strike $\phi = 314^\circ$, dip $\delta = 83^\circ$, and rake $\lambda = 170^\circ$, seismic moment $M_0 = 1.6 \times 10^{18} \text{ N} \cdot \text{m}$ (M_W 6.1), and centroid depth at 15.1 km (<https://www.globalcmt.org/CMTsearch.html>). The Institute of Geophysics, China Earthquake Administration (IGP-CEA) obtained a double-couple solution based on regional broadband station recordings using the Cut and Paste (CAP) method (Bai et al., 2020; Zhu & Ben-Zion, 2013), with strike $\phi = 138^\circ$, dip $\delta = 82^\circ$, rake $\lambda = -161^\circ$, moment magnitude M_W 6.0, and centroid depth at 5.0 km (<https://www.cea-igp.ac.cn/kydt/278248.html>). The CAP method is typically point source moment tensor inversion but with flexible time shifts for different phases (P , S , and Surface waves) at regional distances to account for the inaccurate velocity structure. The grid search can be done for source depth, centroid epicenter location, and centroid time shift.

Given the variations in centroid depth and strike among these solutions, we perform a point-source inversion by the CAP method using the regional broadband recordings from 44 stations of the YN seismic network from ChinArray (Gong et al., 2022; Zheng et al., 2010) mostly within 300 km of the epicenter (Figure 2b). The P and S waveforms are bandpass filtered at 0.02–0.15 Hz and at 0.02–0.10 Hz, respectively. Seismic waveforms of three stations (CHT, TUS, and NAJ) located close to the epicenter are clipped, and cannot be used in waveform inversions. The local seismic velocity model averaged within 200 km of the epicenter adopted from Yang et al. (2020) is used in the CAP inversion. The inversion is summarized in Figure 3. It has a best double-couple for one nodal plane with strike $\phi_1 = 42^\circ$, dip $\delta_1 = 71^\circ$, rake $\lambda_1 = -16^\circ$, and the other nodal plane with strike

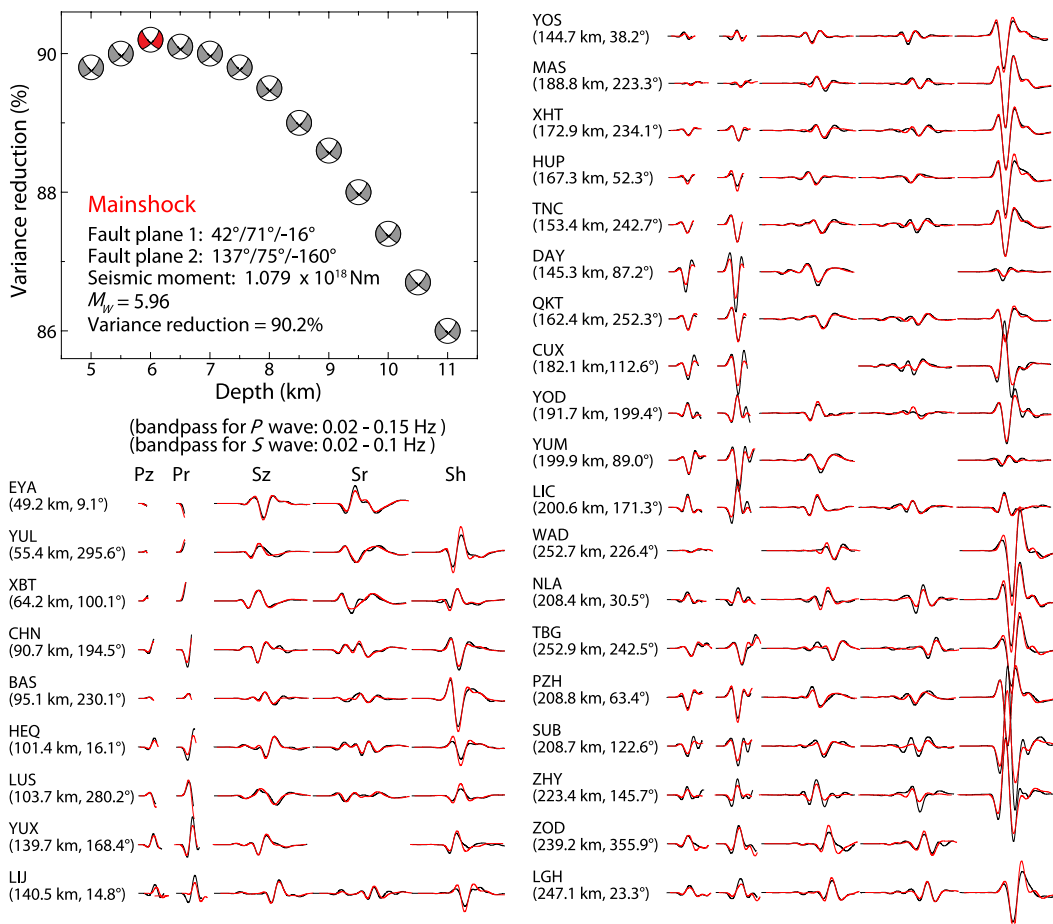


Figure 3. Point-source focal mechanism inversion for the 2021 Yangbi mainshock. The focal mechanism was inverted by the CAP method for point sources varying in depth from 5.0 to 11.0 km. Waveform fitting for the solution at the optimal depth at 6.0 km is shown. The indicated bandpass filters have been applied to the *P* and *S* seismogram segments. The distance (km) and azimuth ($^\circ$) for each station are indicated. Black and red traces show the data and synthetics, respectively. The NW-SE nodal plane is our preferred rupture plane used in further analysis.

$\phi_2 = 137^\circ$, dip $\delta_2 = 75^\circ$, rake $\lambda_2 = -160^\circ$. Considering the northwest-southeast trend of the Yangbi sequence, the plane with strike $\phi = 137^\circ$ and dip $\delta = 75^\circ$ toward the southwest direction, rather than the northeast-trending nodal plane, appears to be the fault plane. The inverted seismic moment M_0 is $1.079 \times 10^{18} \text{ N} \cdot \text{m}$ ($M_w 5.96$), and the optimal search suggests a relatively shallow centroid depth at 6 km (Figure 3). The solution is similar to the IGP-CEA solution based on a similar dataset. The deeper centroid depths of USGS-NEIC (17.5 km) and GCMT (15.1 km) solutions are likely biased by the relatively low signal-to-noise ratio of teleseismic data at long period for this event magnitude and the average global velocity structure used in the inversion.

2.2. Apparent Moment-Rate Functions (AMRFs)

Near-source Green's functions appear to be complicated for periods shorter than those used in the CAP inversions, due to the complex crustal structures around the Yangbi area. The use of simple 1D velocity model Green's functions or low resolution 3D velocity model Green's functions for the shorter periods that provide detailed source information may project structural errors into the inferred rupture process in the source inversion. Therefore, we use the empirical Green's functions (EGFs) method to determine broadband apparent moment-rate functions (AMRFs) of the Yangbi mainshock and then infer the rupture process based on AMRFs following a similar procedure used in Ross et al. (2017, 2018). Two smaller nearby events having similar focal mechanisms to the mainshock (Figures S1 and S2 in Supporting Information S1) are selected as EGF earthquakes to deconvolve broadband recordings and thus remove most propagation and site effects for a given station. The

deconvolution was performed in the time domain without positivity constraints using the procedure of Kikuchi and Kanamori (1982) as updated by Ligorría and Ammon (1999). The two EGF events, EGF1 and EGF2, are both located in the southeast direction from the mainshock epicenter, with EGF2 closer to the mainshock (Figure 2c; based on the YEA catalog, EGF1 and EGF2 are 6.4 and 3.0 km from the mainshock, respectively).

We determine the AMRFs using *SH* waveforms from the transverse components with relatively cleaner waveforms compared to *P* and *SV* waves (Figure S3 in Supporting Information S1). We apply a 1.0 Hz lowpass filter for each EGF event and the mainshock recording windowed starting 10 s before the *P* arrival with various total duration up to a maximum of 110 s (see some waveform examples in Figure S3 in Supporting Information S1). We handpick the *P* arrivals for the mainshock and EGF events, respectively, so the AMRF analysis is little affected by the precise event locations as long as EGF events are located within about the rupture length of the mainshock with little variation in the intra-event velocity structure. The 1.0 Hz lowpass filter operation slightly smooths the AMRFs, but retains sufficient bandwidth to resolve source processes for an M_w 6.0 earthquake. After removing the AMRFs for stations near *SH* radiation nodes, which usually have considerable noise, we have about 30 stations with stable deconvolutions (blue triangles in Figure 2b).

Figures 4 and 5 show the AMRFs and reconstituted waveform fits sorted by azimuth using EGF1 and EGF2, respectively. Because the recordings of EGFs and the mainshock may be cut with inconsistent windows due to minor errors in handpicking *P* arrivals and differences in path effects across the mainshock rupture extent, the onset times of AMRFs from deconvolution are often inconsistent. Therefore, we manually shifted the onset times of AMRFs to align them as indicated in the figures. The AMRFs using EGF1 and EGF2 at different locations relative to the mainshock (Figure 2c) are substantially consistent for each station, and the average variance reductions for waveform fitting are $\sim 90\%$. Both indicate the robustness of the AMRFs we obtained. The source durations of the AMRFs at azimuths between 100° to 140° in the southeast direction, which is proximate to the fault strike, are relatively short (less than ~ 3.0 s), with compact time history. The source durations of AMRFs at azimuths opposite to the strike are longer, up to ~ 7.0 s, and the time history is rougher and spread out. Between these orientations, the source durations change systematically with azimuth.

The azimuthally varying durations and shapes of the AMRFs indicate the directivity of rupture propagation. Initially, we use the duration information to estimate rupture direction, speed, and length of mainshock by assuming an unilateral 1D line source propagating horizontally. The corresponding relation (e.g., Ye, Lay, Zhan, et al., 2016) between duration of AMRFs (T_i), station azimuth (φ_i), rupture direction (φ_r), rupture speed (V_r), and rupture length (L) at the station i is:

$$T_i = \frac{L}{V_r} + \tau_s + \Gamma_i \cdot L \quad (1a)$$

$$\Gamma_i = -p_i \cdot \cos(\varphi_i - \varphi_r) \quad (1b)$$

in which τ_s is source rise time (we assume $\tau_s = 0.7$ s, which is about 10%–20% of the rupture duration L/V_r), Γ_i is rupture directivity parameter, and p_i is ray parameter of the *SH* wave. We can search over different values of rupture direction φ_r to fit the AMRFs using Equation 1a. To stabilize the inversion, we constrain unresolved negative values in the AMRFs to zero in the following analysis.

The AMRFs are well fit by the model with rupture direction $\varphi_r = 137^\circ$, which is equal to the fault strike. Figure 6 shows the AMRFs using EGF1 and EGF2 sorted by directivity parameter with $\varphi_r = 137^\circ$. Because of the uncertainty in the late AMRF energy which could be noise from wave propagation and deconvolution procedure, we plot two estimates of rupture length and speed indicating the upper and lower bounds on rupture speed V_r . The red line is an upper bound with $V_r = 2.2$ km/s and rupture length $L = 8.6$ km, capturing the late AMRF energy well. The blue line is a lower bound with $V_r = 1.5$ km/s and $L = 6.6$ km, capturing the late AMRF energy less well in the rupture direction (the most negative directivity parameters).

2.3. Line-Source Solution

We investigate rupture direction, rupture speed, and rupture length for a line source that is not constrained to be horizontal, but on the fault plane. With this line source assumption, we estimate corresponding moment-rate functions by normalizing the AMRFs to have consistent seismic moment equal to 1.079×10^{18} N · m from the CAP moment tensor inversion and then grid search for the optimal rupture speed and direction. We refer to

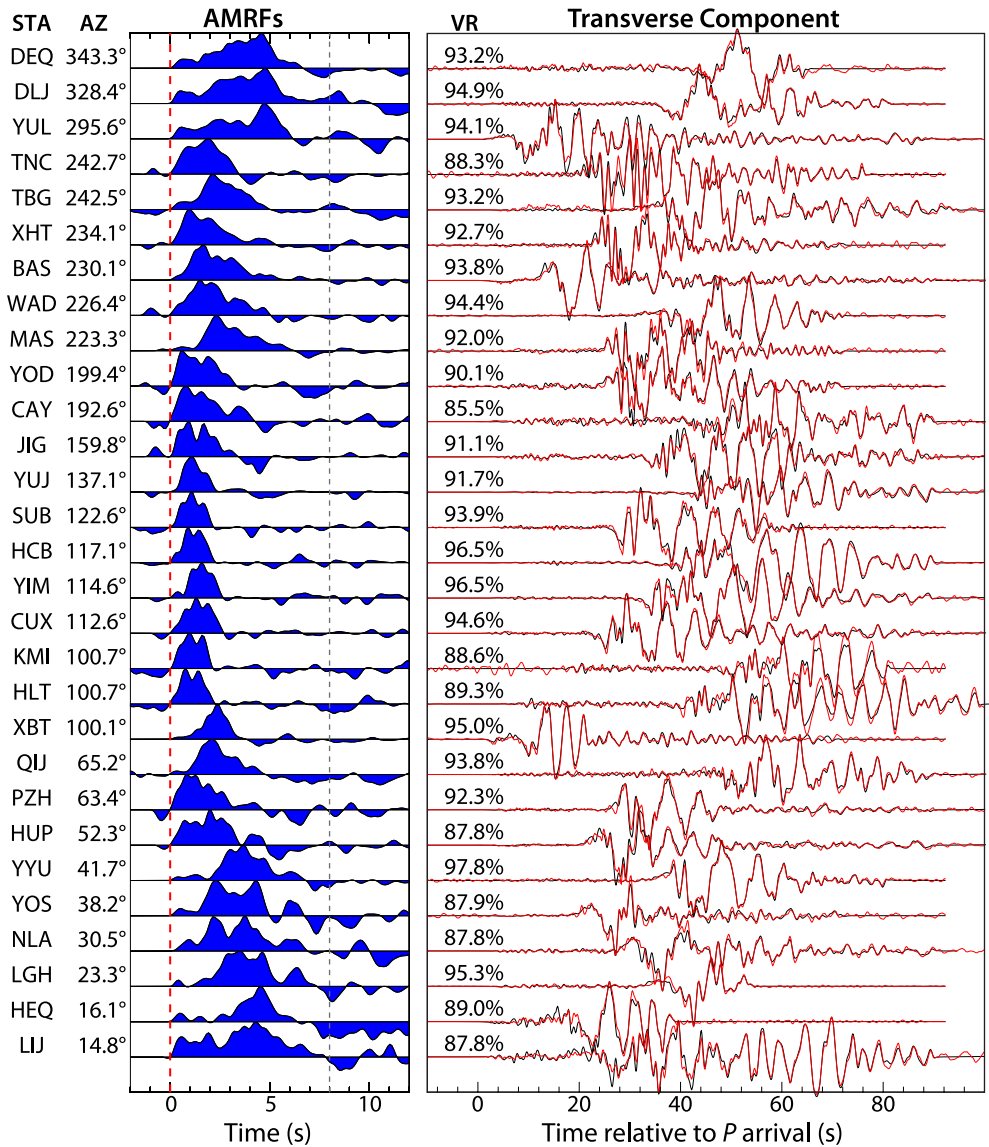


Figure 4. AMRF deconvolutions of SH waves for the mainshock using EGF1 as EGF event with corresponding waveform fits. The deconvolutions were done by the iterative method with a 1 Hz lowpass Butterworth filter. AMRFs are aligned by shifting the onset time to the red dashed line. The dashed gray line indicates the time window used for the 1D and 2D source analysis. In the right panel, red and black curves are synthetic and observed SH waves of the mainshock, respectively, and percentages indicate waveform variance reductions (VR).

the obtained moment-rate functions for this line source as moment-rate line functions (MRLFs) for simplicity. The 1D Radon transform for a line source (Ruff, 1987) is:

$$f(t) = \int_0^L m(t - \Gamma r) dr \quad (2a)$$

$$\Gamma = - \left[\frac{\sin(i_h) \cos(\phi - \varphi) \cos(\lambda)}{\beta} + \frac{\sin(i_h) \sin(\phi - \varphi) \cos(\delta) \sin(\lambda)}{\beta} - \frac{\cos(i_h) \sin(\delta) \sin(\lambda)}{\beta} \right] \quad (2b)$$

$$m(r, t) = 0, \left(t - \frac{r}{V_r} < 0 \right) \quad (2c)$$

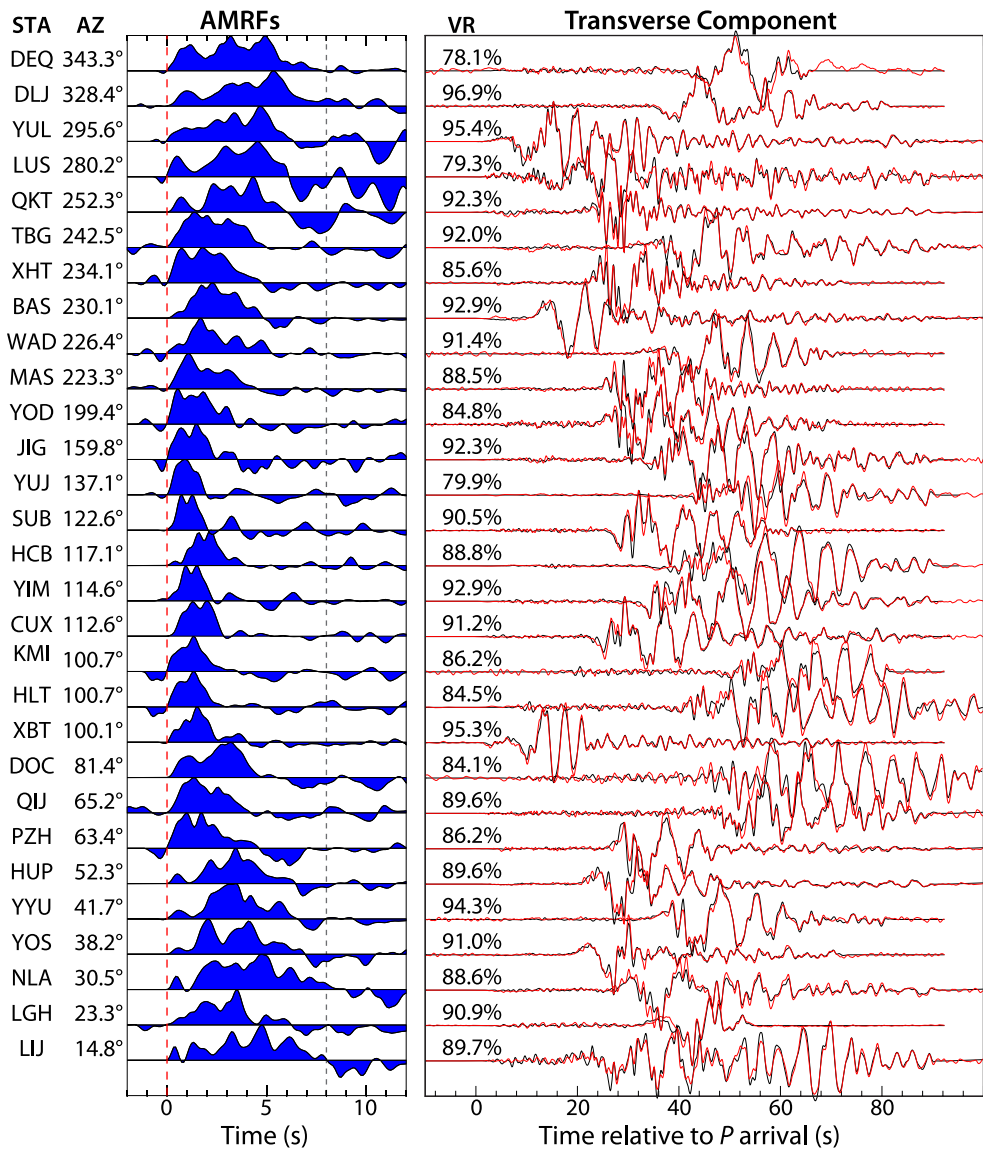


Figure 5. AMRF deconvolutions of SH waves for the mainshock using EGF2 as EGF event and corresponding waveform fitting. The deconvolutions were done by the iterative method with a 1 Hz lowpass Butterworth filter. AMRFs are aligned by shifting the onset time to the red dashed line. The dashed gray line indicates the time window used for the 1D and 2D source analysis. In the right panel, red and black curves are synthetic and observed SH waves of the mainshock, respectively, and percentages indicate waveform variance reductions (VR).

in which Γ , L , and φ are directivity parameter, rupture length and station azimuth, respectively. $f(t)$ are AMRFs, $m(t)$ are MRLFs, i_h is takeoff angle, δ is dip angle, ϕ is strike angle, λ is rupture direction with respect to the fault strike (anti-clockwise) on the fault plane, and β is shear wave velocity near the source which is assumed to be 3.36 km/s (Yang et al., 2020). We perform a non-negative linear least squares (NNLSQ) inversion with $m(t)$ as model and $f(t)$ as data based on Equations 2a-2c. Depending on the maximum duration of AMRFs, the rupture length and the length of MRLFs are prescribed. The faulting geometry with strike $\phi = 137^\circ$ and dip $\delta = 75^\circ$ from our CAP solution is used in the inversion. The late signals in the AMRFs appear to be noise, which could contribute to the seismic moment in the inversion, so we taper them out (Figure 7b). The variance reductions of AMRFs fits for four stations (HEQ, LGH, TNC, and YYU) are lower than 80%, so lower weights of 0.3, compared to 1.0 for other stations, are used for those AMRFs in the inversion.

Figure 7a shows the variance reductions of AMRFs fits for different rupture speeds and rupture direction with respect to the fault strike (anti-clockwise) on the fault plane using AMRFs with EGF1 as the EGF earthquake. The

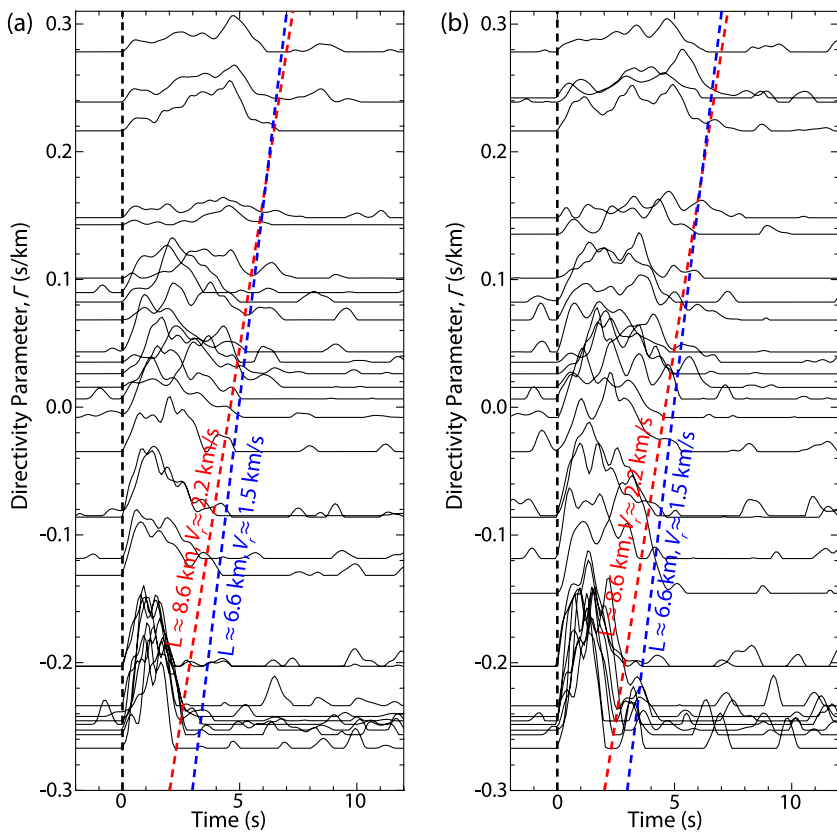


Figure 6. AMRFs of the mainshock ordered by directivity parameter Γ . Directivity parameters for different stations are estimated assuming horizontal rupture along strike (137°). (a) and (b) are the AMRFs using EGF1 and EGF2 as EGF earthquake, respectively. The red and blue dashed lines estimate durations of AMRFs, corresponding to two estimates of rupture length and speed. The blue line for a lower bound on rupture speed captures the late AMRF energy well. The red line for an upper bound on rupture speed captures the late AMRF energy less well.

optimal rupture speed is 2.4 ± 1.1 km/s, and the optimal rupture direction on the fault plane is $333^\circ \pm 44.6^\circ$ with two standard deviations. The variance reduction with the optimal rupture speed and direction is 86.4% (Figure 7b). We get similar results with optimal rupture direction of $340^\circ \pm 53.9^\circ$ and rupture speed of 2.4 ± 1.2 km/s using AMRFs with EGF2 as the EGF earthquake (Figure S4 in Supporting Information S1). Considering the large variance of the rupture speed and direction, we consider the inversion results with different rupture speeds (1.8–2.7 km/s) and directions ($315^\circ - 345^\circ$) around the optimal values (Figure S5 in Supporting Information S1). For $V_r = 1.8$ km/s or $\lambda = 315^\circ$, the MRLFs are too temporally contracted, while for $V_r = 2.7$ km/s, the beginning of MRLFs are not aligned well, and for $\lambda = 345^\circ$, MRLFs are spread in time. Thus, we conclude that rupture speed of 2.1–2.4 km/s and rupture direction of 325° – 335° on the fault plane are reasonable, which indicate that the line source rupture propagates southeastward (azimuth $\sim 144^\circ$) with a rupture length of ~ 8 km.

2.4. 2D Finite-Fault Slip Distribution

With constraints from the 1D line source, we invert the normalized AMRFs for the 2D finite-fault slip distribution on the fault plane with the NNLSQ inversion. The 2D Radon transform for the finite-fault source (Ruff, 1987) is given by:

$$f(t) = \mu \iint \dot{D}(t - \Gamma_s x - \Gamma_d y) dx dy \quad (3a)$$

$$\Gamma_s = -\frac{\sin(i_h) \cos(\phi - \varphi)}{\beta} \quad (3b)$$

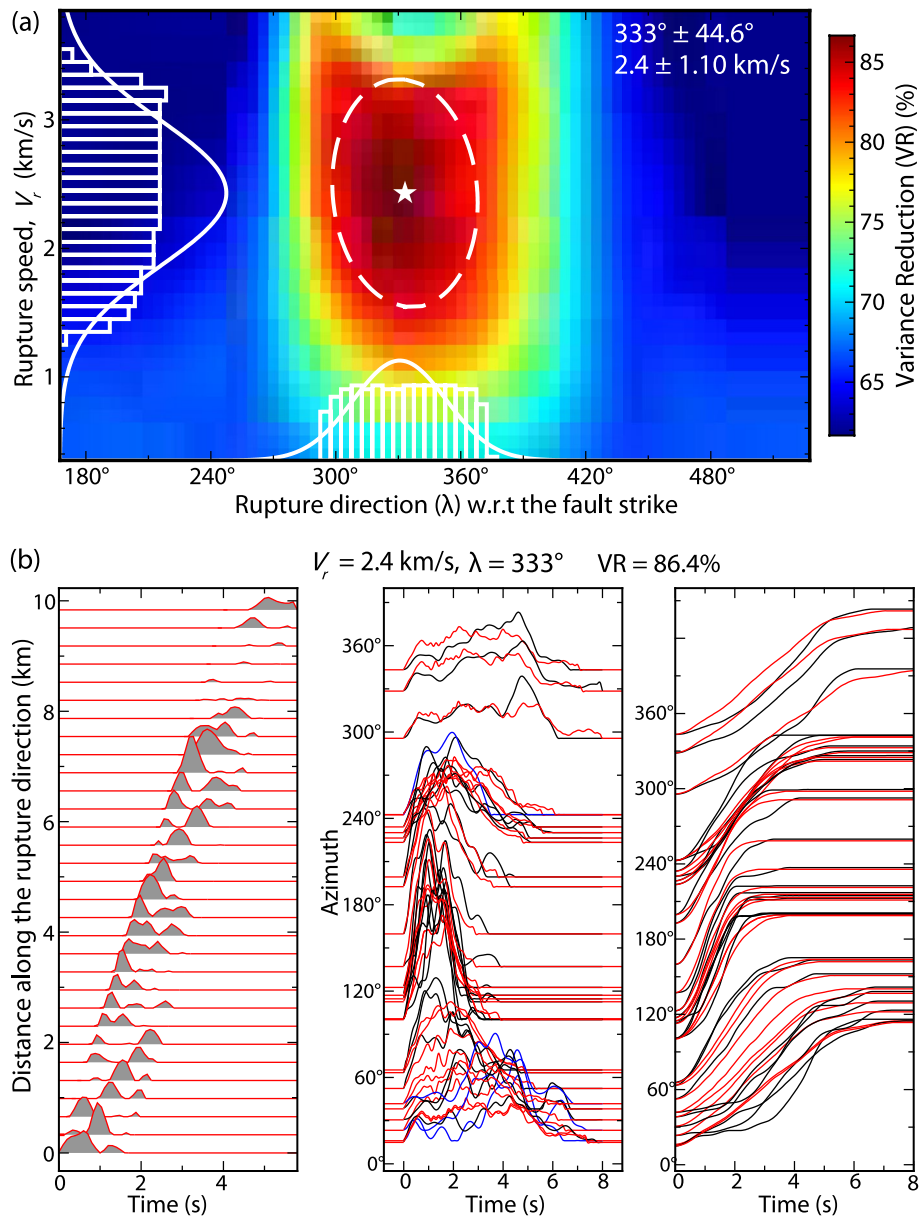


Figure 7. The optimal rupture speed and rupture direction with respect to the fault strike (anti-clockwise) for a line source on the fault plane based on grid search using AMRFs with EGF1 as the EGF earthquake. (a) Variance reductions (VRs) for different rupture speeds and rupture directions on the fault plane (strike = 137° and dip = 75°). VRs larger than $\sim 81\%$ (95% of the maximum of VR) are used to estimate the mean and standard deviation of rupture speed and rupture direction. The dashed ellipse shows 95% confidence. Two histograms show the amount of data with $VR > \sim 81\%$. The optimal (white star) and two standard deviations of rupture speed and rupture direction are indicated by the inset numbers. (b) Results for a line source with the optimal rupture speed and rupture direction. The left panel shows the inverted MRLFs. The middle panel shows the observed (black) and synthetic (red) AMRLFs, and the right panel shows the corresponding moment time histories. Variance reductions of four AMRFs (blue) at HEQ, LGH, YYU, and TNC with increased azimuths are lower than 80%, and the weights of these AMRFs are 0.3 (rather than 1.0) in the inversion.

$$\Gamma_d = \frac{\sin(i_h)\sin(\phi - \varphi)\cos(\delta)}{\beta} - \frac{\cos(i_h)\sin(\delta)}{\beta} \quad (3c)$$

$$\dot{D}(t, x, y), \quad t \in \left(\frac{\sqrt{x^2 + y^2}}{V_r}, \frac{\sqrt{x^2 + y^2}}{V_r} + t_s \right) \quad (3d)$$

in which $\dot{D}(t, x, y)$ is the source slip-rate function; Γ_s and Γ_d are the rupture directivity parameter along strike and along dip, respectively. In the inversion, we set model grid of 0.5-km by 0.5-km with 25 grids along dip and 31 grids along strike with a uniform faulting geometry of strike $\phi = 137^\circ$ and dip $\delta = 75^\circ$. We use a multiple time window linear inversion method to solve for the coseismic slip distribution (Hartzell & Heaton, 1983). The subfault slip-rate functions are parameterized with 10 0.2-s rise-time triangles with 0.2-s offsets, giving total possible subfault durations of 2.2 s. The total seismic moment is constrained to be $M_0 = 1.079 \times 10^{18}$ N · m inverted from the long-period seismic data. Constant shear modulus $\mu = 30$ GPa and $\beta = 3.36$ km/s are used. We perform a NNLSQ inversion with the seismic moment constraint, temporal smoothing, and spatial smoothing having corresponding normalized weights of 0.01, 0.1, and 0.05 in the power of the coefficient matrix by the data matrix. The normalization is defined from the power of the corresponding coefficient matrix. Assume that the inversion problem is written as

$$\begin{bmatrix} G \\ \lambda_1 G_1 \\ \lambda_2 G_2 \\ \lambda_3 G_3 \end{bmatrix} \begin{bmatrix} \bar{m} \end{bmatrix} = \begin{bmatrix} d \\ \lambda_1 M_0 \\ c_0 \\ 0 \end{bmatrix}$$

where G , G_1 , G_2 , and G_3 are coefficient matrix for the moment constraint, temporal smoothing, and spatially smoothing, respectively. Then weights λ_1 , λ_2 , and λ_3 are given by

$$\lambda_1^2 = 0.01 \frac{|G|^2}{|G_1|^2}, \quad \lambda_2^2 = 0.1 \frac{|G|^2}{|G_2|^2}, \quad \lambda_3^2 = 0.05 \frac{|G|^2}{|G_3|^2}.$$

Referring to the estimated rupture speeds in the line source inversion, we use three maximum rupture expansion speeds of 2.0, 2.2, and 2.4 km/s in the inversion.

Figure 8 shows the results of the finite-fault inversions using AMRFs with EGF1 as the EGF earthquake. The main characteristics for the coseismic slip distribution with three maximum rupture expansion speeds (kinematic expansion speed from the hypocenter defining the earliest initiation of each subfault) look consistent with each other, but peak slip (~ 2.4 m, ~ 2.1 m, and ~ 1.6 m) decreases with maximum rupture expansion speed (2.0 km/s, 2.2 km/s, and 2.4 km/s). Figure S6 in Supporting Information S1 shows additional results for maximum rupture expansion speeds from 1.4 km/s to 3.0 km/s with an interval of 0.2 km/s. All slip models have similar moment-rate functions, while the inverted seismic moments slightly deviate from the input value. Their fits for the observed AMRFs are comparable with very slight differences. Here, we mainly focus on the results found for a rupture speed of 2.2 km/s. Rupture propagates to the SE (137°) ~ 8.0 km along strike, and along the down-dip direction ~ 4 km from 8 to 12 km depth. The centroid depth is ~ 10 km with a hypocenter of 8.0 km, and the peak slip is ~ 2.1 m. The duration of the moment-rate function is ~ 6.0 s, and the corresponding centroid time is ~ 2.5 s. Figure S7 in Supporting Information S1 shows the inverted distribution of subfault moment rate functions with the different assumed durations of 1.4–3.0 s with rupture speed of 2.2 km/s. The subfault moment rate is rather stable for regions with large slip. Figure S8 in Supporting Information S1 shows the inverted results using AMRFs with EGF2 as the EGF earthquake. The coseismic slip distributions with three rupture speeds are lower, but consistent in relative size with those using EGF1, with peak slips of ~ 2.1 m, ~ 1.7 m, and ~ 1.4 m, respectively.

2.5. Radiated Seismic Energy Estimates

Following Vassiliou and Kanamori (1982), we can calculate the radiated energy, E_R , by directly integrating the spectra of moment-rate functions.

$$E_R = K M_0^2 I \quad (4a)$$

$$K = [(1/15\pi\rho\alpha^5) + (1/10\pi\rho\beta^5)] \quad (4b)$$

$$I = 8\pi^2 \int_0^\infty f^2 |\hat{s}(f)|^2 df \quad (4c)$$

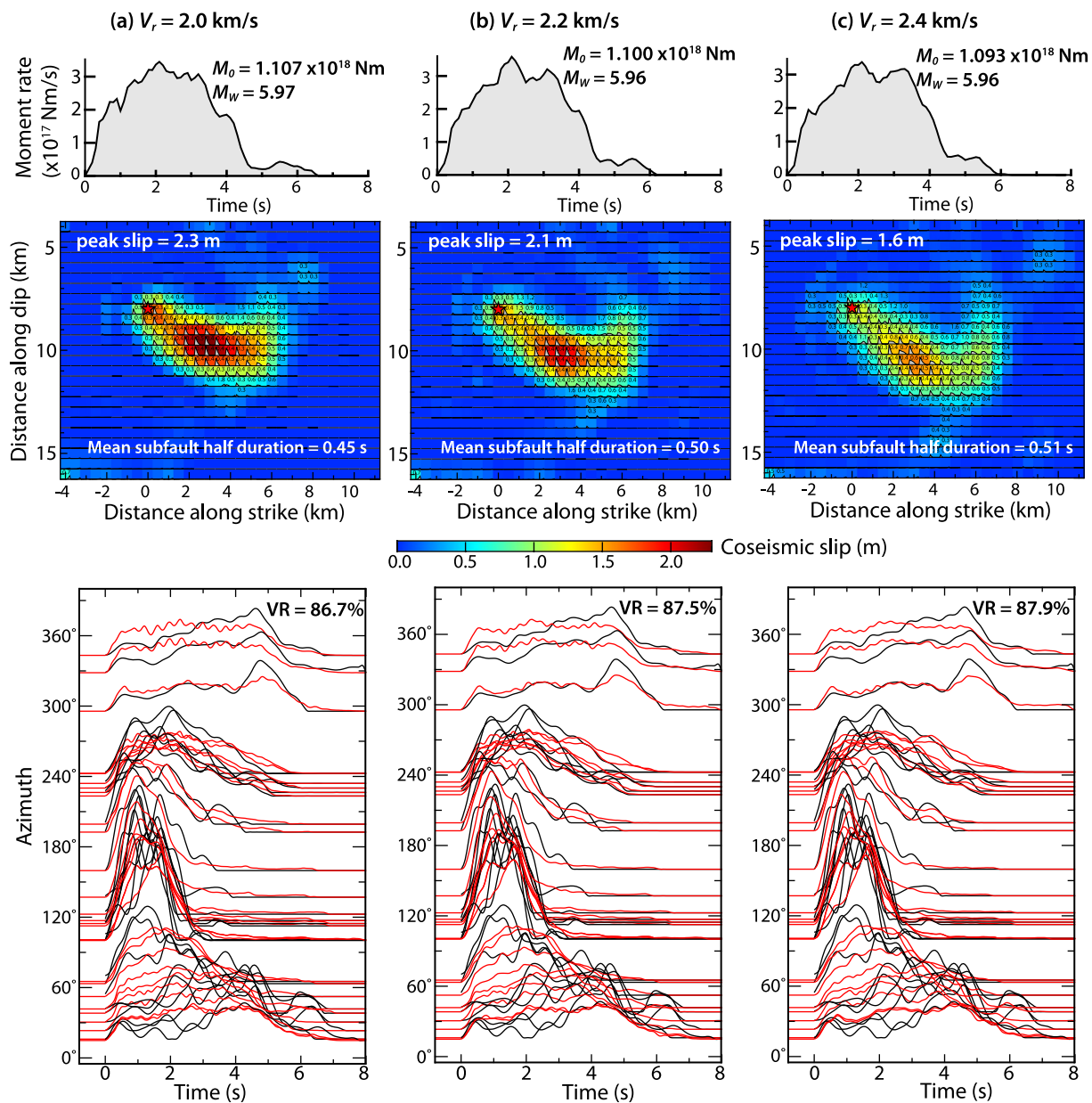


Figure 8. Finite-fault inversions using AMRFs with EGF1 as the EGF earthquake with different assumed rupture expansion speed V_r : (a) $V_r = 2.0 \text{ km/s}$, (b) $V_r = 2.2 \text{ km/s}$, and (c) $V_r = 2.4 \text{ km/s}$. Top panels: moment-rate functions (MRFs); middle panels: coseismic slip distributions with subfault source time functions shown by gray polygons and centroid slip duration marked for those grids with slip larger than 15% of the peak slip; and bottom panels: comparison of synthetic (red) and observed (black) AMRFs.

where $\hat{s}(f)$ is the Fourier transform of the unit source function (moment-rare function with unit area). The P wave velocity α , S wave velocity β , and density ρ at the source are set as 5.70 km/s, 3.36 km/s, and 2.65 g/cm³, respectively. Because we applied a lowpass filter during the deconvolution for AMRFs, the integral in Equation 4c was only calculated up to a value of 1.0 Hz. To account for the missing radiated energy above 1 Hz, we use the Brune source model (Brune, 1970) to extrapolate the source spectrum at the high frequency end.

Figure 9a shows the truncated radiated energy by integrating Fourier spectra of unit AMRFs after excluding negative moment at different azimuths. The truncated radiated energy shows a peak at $\sim 130^\circ$, which is consistent with our rupture directivity, and the median value of E_R is $1.24 \times 10^{13} \text{ J}$. We estimate the corner frequency is $\sim 0.19 \text{ Hz}$ by fitting the average spectra of AMRFs using the Brune model (Figure 9b). For the Brune spectrum with a corner frequency of 0.19 Hz, 23.4% of the radiated energy is above 1 Hz. Thus, by assuming that 23.4%

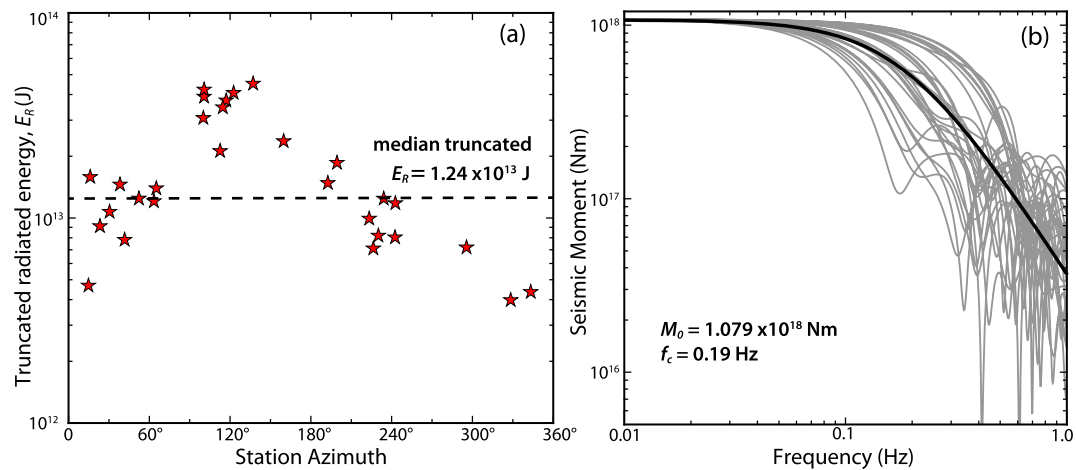


Figure 9. Estimation of radiated energy based on AMRFs. (a) The truncated single-station estimations of radiated energy from AMRFs plotted with station azimuths. The dashed line indicates the median of truncated radiated energy (1.24×10^{13} J). (b) Spectra for AMRFs (gray) and the fitting Brune spectrum (black) with the estimated corner frequency of 0.19 Hz. All spectra are scaled with the seismic moment from the CAP inversion.

of the E_R is missing in the truncated AMRFs, the total radiated energy is estimated to be about 1.62×10^{13} J. The corresponding moment scaled radiated energy E_R/M_0 is 1.5×10^{-5} , which is comparable to the average E_R/M_0 of interplate thrust events of 1.1×10^{-5} (Ye, Lay, Kanamori, & Rivera, 2016), but much smaller than the value of 2.4×10^{-4} for the 2016 M_W 5.2 Borrego Springs earthquake (Ross et al., 2017).

3. Discussion

3.1. Depth Extent of Coseismic Slip

The depth distribution of coseismic slip affects the strong motion shaking and the potential for future faulting, especially for unmapped faults as for the Yangbi sequence (e.g., Ji et al., 2015; Kim & Dreger, 2008). For the 2021 M_W 6.0 Yangbi strike-slip mainshock, directivity analysis (Lei et al., 2021) and published coseismic slip models (e.g., Chen et al., 2022; Yang et al., 2021; Yu et al., 2021; Wang, Liu, et al., 2021; Zhang et al., 2021) all indicate the rupture primarily propagates unilaterally along strike to the southeast, consistent with our result. However, there are discrepancies in the peak slip and the rupture direction along dip, and whether there was some relatively shallow rupture. Based on observations of static displacements from a GNSS network, Zhang et al. (2021) obtain a slip distribution with depths from 3 to 12 km, a peak slip of ~ 1 m, and a centroid depth of less than 10 km but deeper than the hypocenter, suggesting that the rupture slightly propagates downdip. Based on coseismic deformation from Sentinel-1 A/B InSAR data, Yang et al. (2021) invert a slip distribution with an up-dip propagating rupture with depth extent from 2 to 12 km, a peak slip of 0.64 m, and a centroid depth of 7 km. The geodetic inversions suggest shallower slip than our result which has most slip deeper than the assumed hypocenter at 8 km. The inverted coseismic slip using InSAR data contains the contributions of deformation associated with aftershocks, foreshocks and early afterslip, and it is possible that the inferred shallow slip can be attributed to those processes. It is important to evaluate whether the rupture propagated updip or downdip. Our results indicate that the rupture propagated downdip, similar to that of Zhang et al. (2021), but contrasting to that of Yang et al. (2021). By inverting near-source broadband seismic data with 1D synthetic Green's functions, Chen et al. (2022) obtain a slip distribution extending from depths of 3–12 km with the main slip at ~ 7 km updip from the assumed hypocenter of 11 km.

To check the sensitivity of AMRFs to coseismic slip along dip, we calculate synthetic AMRFs for a horizontal mirror image slip distribution along the dip direction relative to the hypocenter, that is, the rupture propagates updip from the hypocenter. The results (Figure 10) show that AMRFs with azimuths from 100° to 250° are quite sensitive to coseismic slip in the along-dip direction, and are not well modeled with the rupture propagating updip. Therefore, we prefer downward propagating rupture along dip. Generally, resolution along dip is not

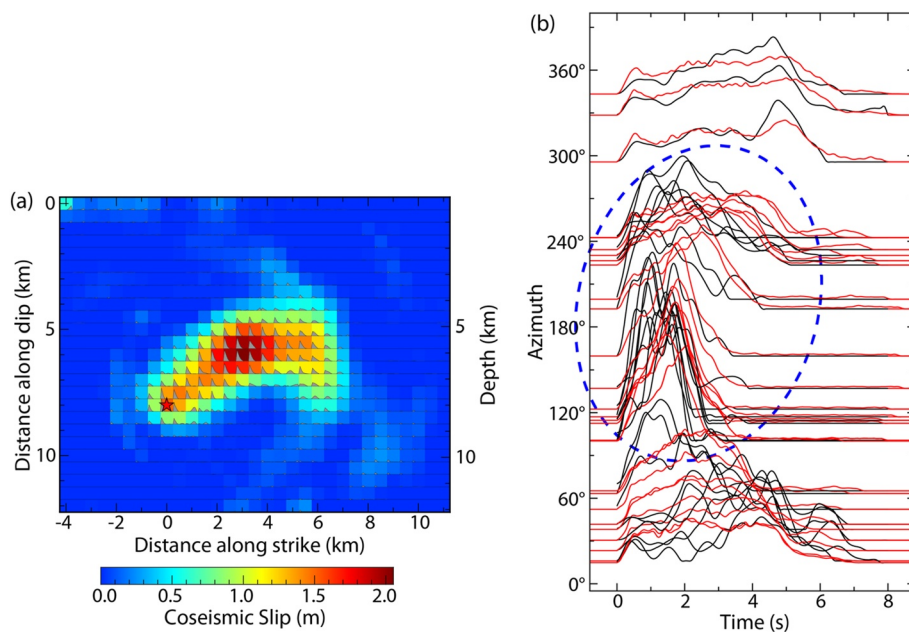


Figure 10. Comparison of observed and synthetic AMRFs for an assumed up-dip rupture. (a) Coseismic slip distribution of up-dip rupture. It is a symmetric distribution relative to the hypocenter along strike direction to our preferred slip model with maximum rupture expansion speed of 2.2 km/s (Figure 8b). The subfault source time functions are shown as gray polygons for those grids with slip larger than 15% of the peak slip. (b) Comparison of observed (black) and predicted (red) AMRFs for the assumed up-dip rupture. In the azimuths of 100°–250°, there are large discrepancies between the predicted and observed AMRFs, highlighted by the blue dashed circle.

constrained well if only seismic data are used, especially for teleseismic waves having narrow ranges of directivity parameters. But the near-source station recordings used in this study to calculate AMRFs have relatively wide ranges of directivity parameters, increasing the sensitivity to coseismic slip along dip. With the hypocenter located at ~10 km (8 km from the YEA catalog; 10 km from the CENC catalog with limited solution; 6.69 km from the high-resolution catalog by Zhou et al. (2021), and 11 km relocated using handpicked P arrivals by Chen et al., 2022), the main slip during the M_w 6.0 Yangbi mainshock is likely to be at depths around 6–12 km and any shallow slip is minor.

3.2. Spatial Distribution of Coseismic Slip With Foreshock/Aftershock Activity

Locations of the 2021 Yangbi sequence from the YEA catalog are preliminary and have significant scatter (Figure 2c and Figure S12 in Supporting Information S1). To evaluate the relative spatial distribution between the main slip area for the mainshock and foreshock/aftershock seismicity, we determine the relative location to the mainshock for four important earthquakes, EGF1, EGF2, the largest foreshock (E3; M_s 5.6), and the largest aftershock (E4; M_s 5.3), and compare our results with other high-resolution relocation results. We use the grid-search method to find the minimum error between the observed and computed P wave travel time differences between the target earthquake and the mainshock (Figures S9 and S10 in Supporting Information S1). Relative to the mainshock epicenter, the relocations of EGF1 and EGF2 are in the southwest direction from the original locations, placing them closer to the slip region of the mainshock (Figure 11 and Figure S11). The location of E3 changed very little, while the relocation of E4 is further southeast from the mainshock. These results are consistent with those of Zhou et al. (2021), except a large discrepancy for EGF2. These relocations have no impact on the foregoing AMRF analysis, given the alignment adjustments made to the deconvolved signals. Instead, the vicinity between the main slip area of the mainshock and EGF events (Figure 11) suggests the recordings from the two EGF events provide good representation of the Green Function along path, especially from the EGF1 event.

In the 2021 Yangbi sequence, most of the foreshocks and aftershocks, including the four relocated earthquakes, are distributed near the periphery of the main slip area of the mainshock, although the locations have large uncertainties (Figure S11 in Supporting Information S1). The relocation results of some studies (Long et al., 2021;

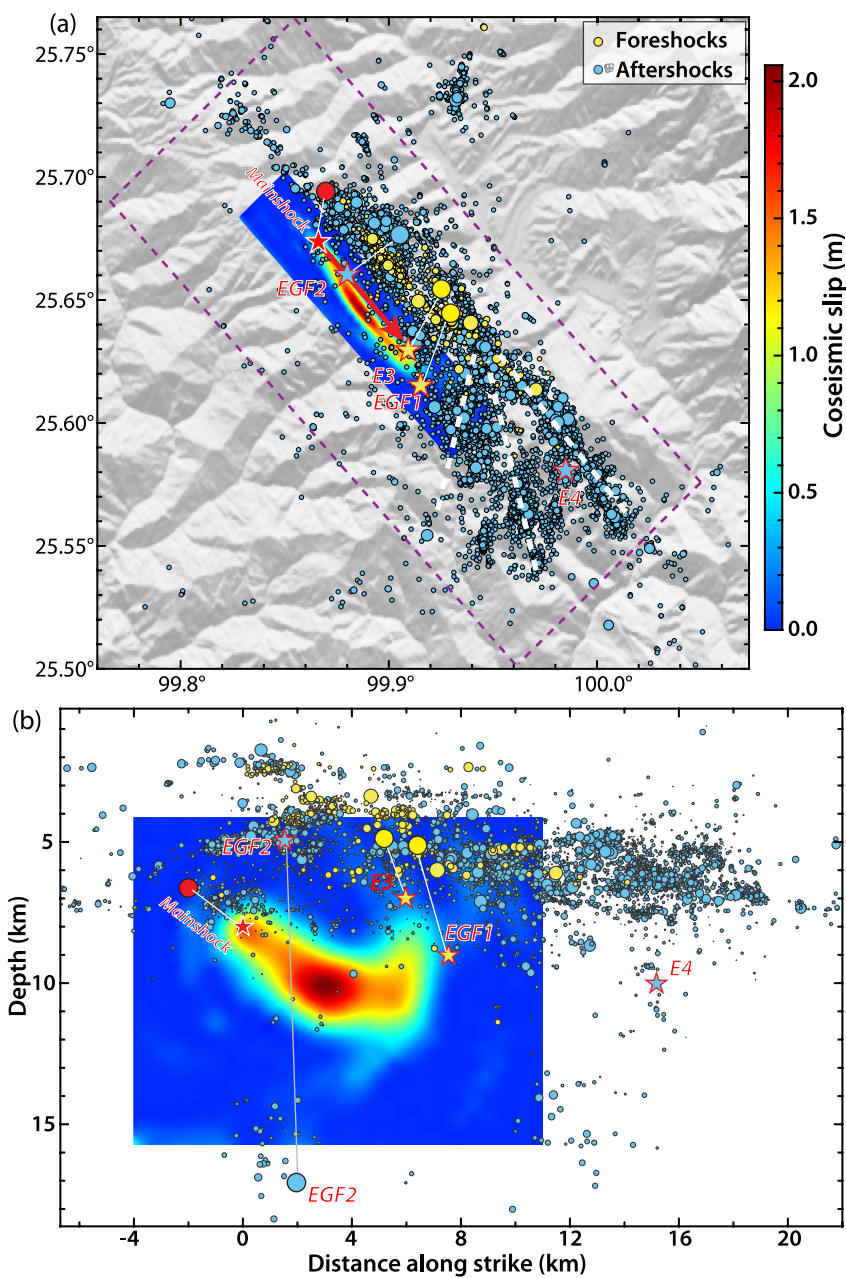


Figure 11. Spatial distribution of our preferred coseismic slip model for the mainshock and foreshock and aftershock activity. (a) Our preferred coseismic slip distribution of the Yangbi mainshock (Figure 8b) and the high-resolution catalog from Zhou et al. (2021). Yellow and blue circles indicate foreshocks and aftershocks from Zhou et al. (2021), respectively. White dashed lines indicate inferred three bifurcating faults. (b) Depth view of the coseismic slip distribution and seismicity in magenta dashed box in (a) along the fault strike. Stars show the mainshock from the YEA catalog, and our relocated EGF1, EGF2, E3, and E4, with bars connecting the corresponding locations from Zhou et al. (2021). E4 is missing in the catalog from Zhou et al. (2021). Our finite-source analysis is insensitive to the absolute locations, so the overall slip pattern of rupture extent would stay stable while the absolute placement of slip distribution would change with the position of the mainshock hypocenter.

Su et al., 2021; Zhang et al., 2022; Zhou et al., 2021) have shown that foreshocks and aftershocks are mainly shallower than the mainshock, indicating that coseismic slip with a down-dip rupture may extend deeper than the foreshock and aftershock area. The augmented catalog of Zhou et al. (2021) suggests a southeastward deepening of the foreshock and the early aftershock sequence similar to the our slip model in Figure 8, but at shallow depths from 3 to 6 km (Figure 11). We infer that the main slip area of the mainshock has a relatively low density

of foreshocks and aftershocks. This suggests that the largest foreshocks on the periphery of the slip area might have triggered the mainshock, and then the mainshock released significant stress in the slip area, leading to a lack of foreshocks and aftershocks within the main slip area. Long et al. (2021) and Zhang et al. (2022) suggest that there are three bifurcating subfaults in the southeastern part of the sequence. Figure 11 also shows that the rupture propagation of the mainshock stopped near the location of the largest foreshock, where the bifurcation starts, indicating that the bifurcating subfaults may have diffused the stress and prevented further rupture propagation toward the southeast.

The 2021 Yangbi sequence struck a region with no mapped fault on the surface and had some conjugate aftershock trends and parallel strands, similar to the 2019 Ridgecrest sequence that occurred on a relatively immature fault (Liu et al., 2019). The relatively low moment scaled radiated energy of the mainshock $E_R/M_0 = 1.5 \times 10^{-5}$ is also similar to the 2019 $M_W 7.1$ Ridgecrest earthquake with $E_R/M_0 = 1.1 \times 10^{-5}$ based on radiated energy measurement from IRIS (Incorporated Research Institutions for Seismology EQEnergy), which might be the result of an immature fault rupture with high fracture energy dissipation. Highly localized ruptures on mature faults with large cumulative offsets can lead to supershear rupture (e.g., Perrin et al., 2016), whereas lower rupture velocity (<1.5 km/s) may be expected for immature faults (Liu et al., 2019). The rupture velocity for the 2021 Yangbi event is relatively typical, as about 2.2 km/s, but the rupture length of 8 km is very short and not many jogs and obstacles may exist on this scale to slow the overall rupture speed. The intense foreshock and aftershock activity for the Yangbi event is similar to the 2019 Ridgecrest sequence and may reflect the presence of many irregularities along an immature fault zone, particularly at the ends of the fault system where multiple fault strands have activated aftershocks. These characteristics suggest that the 2021 Yangbi sequence occurred on a reactivated immature fault, but the lack of surface rupture and unknown history of any prior faulting limit characterization of maturity of the structure as can be performed for mapped faults and damage zones (e.g., Klinger et al., 2018; Manighetti et al., 2007; 2021; Milliner et al., 2016; Pennington et al., 2022; Rodriguez Padilla et al., 2022).

4. Conclusions

The 2021 Yangbi sequence is mainly distributed along a northwest-southeast trend on an unmapped fault. For an assumption of a horizontal 1D line source, the rupture of the mainshock propagated toward the southeast (137°) with a rupture length of 6.6–8.6 km and a rupture speed of 1.5 km/s – 2.2 km/s. A line source inversion within the fault plane indicates that rupture propagates southeast ($\sim 144^\circ$) with a rupture length of ~ 8 km and a rupture speed of 2.1 km/s - 2.4 km/s. Coseismic slip inversion on the 2D fault plane indicates that rupture propagated along strike over ~ 8.0 km and ~ 5 km downdip with a peak slip of ~ 2.1 m and centroid time (half duration) of ~ 2.5 s. The rupture propagation stopped near the largest foreshock, where three bifurcating faults have been inferred, indicating that the bifurcating subfaults might have dispersed stress and blocked the southeastward rupture propagation. Foreshocks and aftershocks are distributed near the periphery of the main slip area, particularly at shallower depth suggesting substantial release of stress in the large slip area. The relatively low moment scaled radiated energy of the 2021 Yangbi mainshock, high foreshock productivity, and aftershocks activating multiple fault strands at the end of the fault system may be the result of reactivation of an immature fault, similar to the 2019 Ridgecrest sequence.

Data Availability Statement

Waveform data for this study are provided by Youjin Su and Lan Sun from Yunnan Earthquake Agency and Data Management Center of China National Seismic Network at Institute of Geophysics, China Earthquake Administration (SEISDMC, <http://doi.org/10.11998/SeisDmc/SN>, <http://www.seisdmc.ac.cn>). The continuous waveform data can be requested with a preauthorized account from the Data Management Center of China Seismic Network. The raw waveform data to reproduce results in this study are accessible via GitHub (https://github.com/WenzhengGong/2021_Yangbi_data; <https://doi.org/10.5281/zenodo.6767037>). Earthquake information is based on the catalogs provided by Yunnan Earthquake Agency (referred as the YEA catalog), the National Earthquake Data Center at China Earthquake Network Center (CENC-NEDC; https://data.earthquake.cn/dashshare/report.shtml?PAGEID=earthquake_zhengshi) and the U.S. Geological Survey National Earthquake Information Center (USGS-NEIC; <https://earthquake.usgs.gov/earthquakes>). The Global Centroid Moment Tensor (GCMT) solution is from <https://www.globalcmt.org/CMTsearch.html>. Active faults data are from China Earthquake Data Center (<http://dashshare.igl.earthquake.cn/map/ActiveFault/introFault.html>).

- Wang, Y., Wang, E., Shen, Z., Wang, M., Gan, W., Qiao, X., et al. (2008). GPS-constrained inversion of present-day slip rates along major faults of the Sichuan-Yunnan region, China. *Science in China - Series D: Earth Sciences*, 51(9), 1267–1283. <https://doi.org/10.1007/s11430-008-0106-4>
- Wang, Y., Zhao, T., & Hu, J. (2021). Relocation and focal mechanism solutions of the 2021 Yangbi, Yunnan M_s 6.4 earthquake sequence. *Seismology and Geology*, 43(4), 847–863.
- Yang, J., Wen, Y., & Xu, C. (2021). The 21 may 2021 M_s 6.4 Yangbi (Yunnan) earthquake: A shallow strike-slip event rupturing in a blind fault. *Chinese Journal of Geophysics*, 64(9), 3101–3110.
- Yang, Y., Yao, H., Wu, H., Zhang, P., & Wang, M. (2020). A new crustal shear-velocity model in Southwest China from joint seismological inversion and its implications for regional crustal dynamics. *Geophysical Journal International*, 220(2), 1379–1393.
- Ye, L., Lay, T., Kanamori, H., & Rivera, L. (2016). Rupture characteristics of major and great ($M_w \geq 7.0$) megathrust earthquakes from 1990 to 2015: 1. Source parameter scaling relationships. *Journal of Geophysical Research: Solid Earth*, 121(2), 826–844. <https://doi.org/10.1002/2015jb012426>
- Ye, L., Lay, T., Zhan, Z., Kanamori, H., & Hao, J. L. (2016). The isolated~680 km deep 30 may 2015 M_w 7.9 Ogasawara (Bonin) Islands earthquake. *Earth and Planetary Science Letters*, 433, 169–179. <https://doi.org/10.1016/j.epsl.2015.10.049>
- Yu, S., Luo, J., Yang, Y., & Li, C. (2021). Seismogenic structure of the Yangbi, Yunnan M_s 6.4 earthquake on May 21, 2021 constrained by InSAR data. *China Earthquake Engineering Journal*, 43(4), 777–783.
- Zhang, K., Gan, W., Liang, S., Xiao, G., Dai, C., Wang, Y., & Ma, G. (2021). Coseismic displacement and slip distribution of the 2021 May 21, M_s 6.4, Yangbi earthquake derived from GNSS observations. *Chinese Journal of Geophysics*, 64(7), 2253–2266.
- Zhang, P., Deng, Q., Zhang, Z., & Li, H. (2013). Active faults, earthquake hazards and associated geodynamic processes in continental China. *Scientia Sinica Terra*, 43(10), 1607–1620.
- Zhang, Y., An, Y., Long, F., Zhu, G., Qin, M., Zhong, Y., et al. (2022). Short-term foreshock and aftershock patterns of the 2021 M_s 6.4 Yangbi earthquake sequence. *Seismological Research Letters*, 93(1), 21–32. <https://doi.org/10.1785/0220210154>
- Zheng, X., Yao, Z., Liang, J., & Zheng, J. (2010). The role played and opportunities provided by IGP DMC of China National Seismic Network in Wenchuan earthquake disaster relief and researches. *Bulletin of the Seismological Society of America*, 100(5B), 2866~2872–2872. <https://doi.org/10.1785/0120090257>
- Zhou, Y., Ghosh, A., Fang, L., Yue, H., Zhou, S., & Su, Y. (2021). A high-resolution seismic catalog for the 2021 M_s 6.4/ M_w 6.1 Yangbi earthquake sequence, Yunnan, China: Application of AI pickeer and matched filter. *Earthquake Science*, 34. <https://doi.org/10.29382/eqs-2021-0031>
- Zhu, L., & Ben-Zion, Y. (2013). Parametrization of general seismic potency and moment tensors for source inversion of seismic waveform data. *Geophysical Journal International*, 194(2), 839–843. <https://doi.org/10.1093/gji/ggt137>